Electron Tug Effect in Ni Single Atoms for Carbon Dioxide Electroreduction over a Wide Potential Range

Xu Han,[a,b] Ting Zhang,[a,b]* Chao Yue Zhang,[b] Martí Biset-Peiró,[b] Ke Xiao,[b] Pengfei Cao,[c]* Marc Heggen,[c] Weiqiang Tang,[d]* Miquel Vega-Paredes,[e] Alba Garzón Manjón,[a] Lirong Zheng,[f]* Rafal E. Dunin-Borkowski,[c] Andreu Cabot,[b,g] Kim Daasbjerg,[h,i] Joan Ramon Morante,[b,j] Jordi Arbiol[a,g]*

[a]Catalan Institute of Nanoscience and Nanotechnology (ICN2), CSIC and BIST, Campus UAB, Bellaterra, Barcelona, 08193, Catalonia, Spain

[b]Catalonia Institute for Energy Research (IREC), Jardins de les Dones de Negre 1, Sant Adrià del Besòs, Barcelona, 08930, Catalonia, Spain

[c]Ernst Ruska-Centre for Microscopy and Spectroscopy with Electrons and Peter Grünberg Institute, Forschungszentrum Jülich GmbH, Jülich, 52425, Germany

[d]State Key Laboratory of Chemical Engineering and School of Chemical Engineering, East China University of Science and Technology, 200237 Shanghai, China

[e]Max-Planck-Institutfur Eisenforschung GmbH (MPIE), 40237, Dusseldorf, Germany

[f]Beijing Synchrotron Radiation Facility, Institute of High Energy Physics, Chinese Academy of Sciences, Beijing, 100049, P. R. China

[g]ICREA, Pg. Lluís Companys 23, Barcelona, 08010, Catalonia, Spain

[h]Department of Chemistry/Interdisciplinary Nanoscience Center (iNANO) Aarhus University Langelandsgade 140, 8000 Aarhus C, Denmark

[i]Novo Nordisk Foundation (NNF) CO_2 Research Center (CORC), Aarhus University, Gustav Wieds Vej 10C, 8000 Aarhus C, Denmark

[j]Department of Physics, Universitat de Barcelona, Barcelona, 08028, Catalonia, Spain

*Correspondence: tingzhang@chem.au.dk

*Correspondence: p.cao@fz-juelich.de

*Correspondence: wqtang@ecust.edu.cn

*Correspondence: zhenglr@ihep.ac.cn

*Correspondence: arbiol@icrea.cat

Abstract

Atomically dispersed symmetrical NiN_4 moieties represent a promising category of catalysts for electrochemical reduction of carbon dioxide (eCO_2RR). Nonetheless, their practical application is constrained by challenges such as high overpotentials and limited potential ranges. Here, we report Ni active sites with unique electron distribution realized by minute amounts of Au nanoparticles decoration and lateral oxygen coordination (Au/Ni-N-O-C) for achieving a low overpotential while widening the applied potential ranges. The optimized $Au_{0.5}$/Ni-N-O-C catalyst exhibits an outstanding eCO_2RR performance, achieving over 95% Faradaic efficiency (FE) of CO within a broad potential window from −0.50 to −0.85 V vs. reversible hydrogen electrode, notably, 93% FE_{CO} at an overpotential of 340 mV. Theoretical calculations demonstrate that additional electron tug effect on Ni single atoms, induced by the oxygen in the lateral coordination configuration and introduced Au nanoparticles, effectively lower the free energy for *COOH formation by redistributing the electronic distribution of Ni active sites, thus significantly promoting the eCO_2RR across a wide applied potential range. This strategy not only presents an efficient pathway to regulate the electron distribution of single atom catalysts, but also is potentially adaptable for diverse catalytic reactions.

Keywords: single atom catalysts, electron tug effect, CO_2 electroreduction, high CO selectivity, wide potential range, Au nanoparticles

Introduction

The electrochemical reduction of carbon dioxide (eCO_2RR) using renewable electricity has emerged as a promising avenue to address anthropogenic CO_2 emissions and combat the global energy crisis.[1-3] Considering the cost of electricity and separation, and the potential value in downstream synthesis through Fisher-Tropsch chemistry, carbon monoxide (CO) is regarded as an economically viable choice among the potential eCO_2RR products.[4,5] However, the formidable activation barrier of the C=O bond in CO_2, alongside the competitive hydrogen evolution reaction (HER), hinder its practical application.[5,6] Hence, the quest for a catalyst displaying both suitable activity and selectivity becomes pivotal for the practical realization of CO_2-to-CO conversion.

Recent attention has turned to *d*-block carbon-supported single-atom catalysts (SACs), a prototypical MN_4 moiety with a local planar-like D_{4h} symmetry, which can activate CO_2 molecules due to their rich *d*-orbital electrons transferring to the unoccupied π^* orbital of CO_2, showing promise in eCO_2RR activity and selectivity.[7-9] Of particular interest is the dispersed NiN_4 site, which significantly reduces the energy barrier for *CO desorption during eCO_2RR, leading to a high selectivity toward CO production compared to other MN_4 species such as CoN_4 or FeN_4.[10-12] Nevertheless, the pristine NiN_4-active site characterized with a highly symmetrical electron configuration demands higher overpotentials to promote the adsorption of reactants and *COOH intermediates in CO_2-to-CO transformation.[13] The higher overpotential represents the higher energy required beyond the thermodynamically necessary level, thus impeding

potential applications.[14-16] Consequently, substantial efforts have focused on reducing the free energy barriers for *COOH intermediates formation via regulating electronic configuration of highly structure-symmetric NiN_4.[17-19] The coordination environment engineering, such as altering the coordination numbers (NiN_x, x<4),[20,21] substituting N atoms with other heteroatoms (S[22] or P[23]), or introducing axial coordination atoms (N,[24] O[25] or Cl[26]), have been explored to break the planar symmetry of NiN_4 and tune the electron distribution around Ni sites. Furthermore, incorporating functional groups[27] or nanoparticles[28,29] on the substrate can also adjust the electronic symmetry, by regulating the metal-substrate electronic conjugation, impacting the electronic polarization of NiN_4. However, employing a sole strategy involving the distortion of electronic density or alteration of the *d*-band center is limited and inadequate, thereby diminishing the effectiveness of optimization for a low overpotential and a wide potential range. Thanks to the spatial and functional compatibility of each regulatory strategy, combining both approaches could effectively redistribute electronic configuration around the Ni centers at different hierarchical scope. More importantly, diverse strategies superimposed on the same active site will form additional electron tug effect, resulting in a unique electron distribution. This distortion of electronic structure could facilitate the adsorption and activation of reactive intermediates and achieve high CO_2 reduction activity and selectivity.

In this work, Ni single atom catalyst with a distinctive electron distribution induced by the electron tug effect have been developed for eCO_2RR. This effect is achieved by combining O planar coordination with nearby gold nanoparticles. Because of different

electronegativity of oxygen atoms, the engineered NiN_3O sites—where a nitrogen atom is substituted with an oxygen atom in the lateral plane—could enhance the charge transfer capability, thus facilitating *COOH formation. Additionally, through the integration of Au nanoparticles, the electron transfer and electron induced effect will significantly manipulate the local geometric and electronic structure of the prepared NiN_3O sites. The formed electron tug effect in this catalytic system will redistribute the electron around local structure to reduce the energy barriers for *COOH intermediate formation on Ni sites, contributing to an enhanced catalytic capability of Ni SACs in eCO_2RR. Particularly, by rationally controlling the amount of Au additive in a unique Ni SAC (NiN_3O), the optimized $Au_{0.5}$/Ni-N-O-C sample exhibited remarkable eCO_2RR performance, maintaining above 95% Faradaic efficiency of CO across a wide potential range from −0.50 to −0.85 V vs. RHE (notably, 93% at an overpotential of 340 mV), which can well meet the requirements for the following CO dimerization or protonation. Moreover, *in-situ* attenuated total reflection infrared (ATR-IR) spectroscopy and theoretical calculations indicate that the superior performance of Au/Ni-N-O-C can be attributed to the additional electron tug effect induced by the O coordination configuration and the presence of gold nanoparticles, which can facilitate the adsorption energies of the *COOH intermediate by shortening the distance between Ni centers and *COOH, resulting in enhanced activity and selectivity for CO production in $Au_{0.5}$/Ni-N-O-C.

2. Results and discussion

2.1 Theoretical calculations

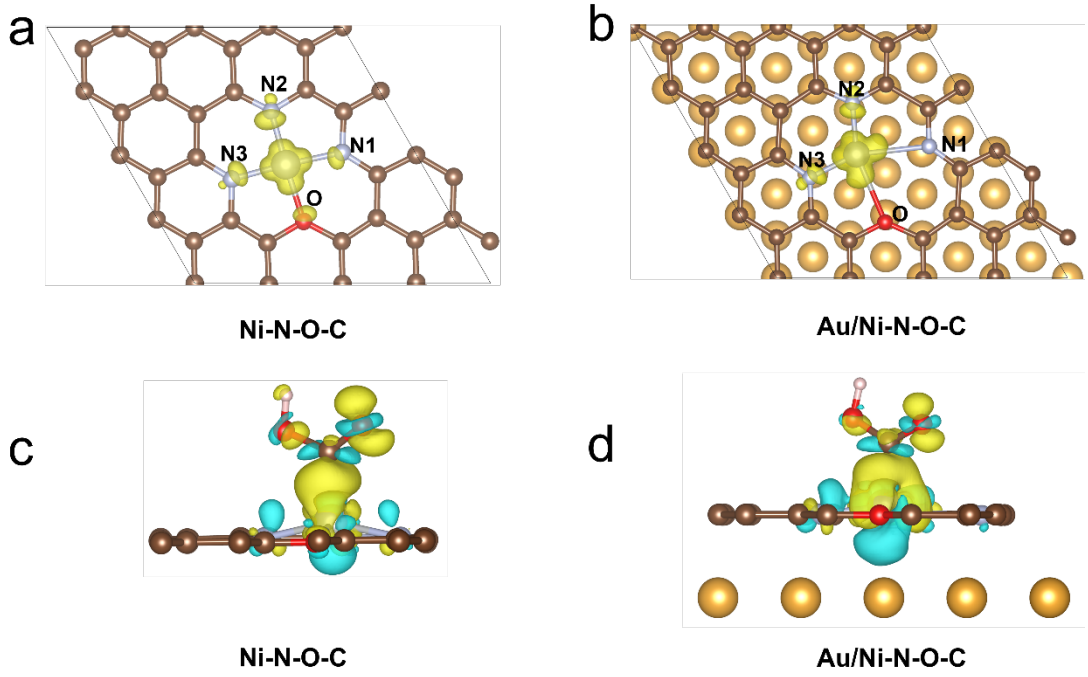

Fig. 1. Theoretical calculations. a, b The atomic structures and spin density plots of **a** Ni-N-O-C and **b** Au/Ni-N-O-C (top view). **c, d** The charge density difference mappings for *COOH on the **c** Ni-N-O-C and **d** Au/Ni-O-C (front view, the yellow and cyan regions represent electron accumulation and depletion, respectively).

To gain a theoretical understanding of the impact of substituting an O atom on electron distribution, two configurations of a Ni atom embedded in a graphene monolayer sheet were studied. One configuration involved the bonding of the Ni atom with four N atoms (NiN_4), while the other configuration involved the bonding with three N atoms and one O atom (Ni-N-O-C) (Fig. 1a and Supplementary Fig. 1a). When a more electrophilic O atom[30] forms a bond with Ni to create a Ni-O bond with a length of 1.986 Å, the lengths of the other Ni-N bonds undergo alterations, introducing variability and disrupting the perfect symmetry of NiN_4 (Supplementary

Table 1). Upon altering the coordination environment, a redistribution of electronic density occurs around the Ni center (Fig. 1a). Introducing Au nanoparticles onto the simulated Ni-N-O-C structure (Fig. 1b) resulted in Ni center displacement from the N-C plane (0.25 Å) with further elongated Ni-N and Ni-O bonds (Supplementary Table 1) and the electron transfers from the Au particles to Ni single atom (Supplementary Table 2). Subsequently, the distorted geometric out-of-plane configuration, coupled with electronic interactions, will create a novel electron tug effect around local structure. This effect, in turn, will instigate the refinement of electron distribution around the active center which is supposed to intensify the interaction with the adsorbed *COOH intermediate. To delve into the structural advantage within electron tug effect in CO_2-to-CO conversion, charge density difference mappings of adsorbed *COOH on normal NiN_4, Ni-N-O-C and Au/Ni-N-O-C were examined (Supplementary Fig. 1b and Fig. 1c, d). The charge accumulation and deficit between *COOH and the corresponding catalyst surface were presented, indicating the adsorption of *COOH on the catalyst surface via electronic interaction. The introduction of Au nanoparticles onto the Ni-N-O-C structure facilitated a more pronounced charge transfer. This indicated that electrons of Ni centers on the Au/Ni-N-O-C catalyst were transferred to *COOH, enhancing the interaction of *COOH with Ni active site. The distance between the Ni atom in the NiN_4, Ni-N-O-C, and Au/Ni-N-O-C catalysts, and the C atom in the adsorbed *COOH were measured as 1.95 Å, 1.95 Å, and 1.84 Å, respectively. The shorter Ni-C bond in the Au/Ni-N-O-C configuration accelerated the charge transfer and strengthened the interaction between

the active site and *COOH, significantly reducing the energy barrier for *COOH formation and enhancing the catalytic activity. These findings highlight that the electron tug effect, achieved by combing O-coordination and Au particle introduction, can effectively modify the geometric and electronic structure, resulting in an improved electrocatalytic activity in Ni SAC systems.

2.2 Synthesis and Characterizations of Different Catalysts

To validate the theoretical findings, Au/Ni-N-O-C was synthesized following the procedure outlined in Fig. 2a. Initially, a Ni-doped IRMOF-3 was prepared by a two-step method, leveraging a pore confinement effect. This prepared Ni-doped IRMOF-3 retained the original crystallinity, functional groups, and morphology of IRMOF-3, as confirmed through X-ray diffraction patterns (XRD), Fourier-transform infrared (FTIR) and field emission scanning electron microscope (FE-SEM) analyses (Supplementary Figs. 2-4). Subsequently, the Ni-N-O-C catalyst was obtained via simple pyrolysis under an Ar atmosphere, which then acted as a substrate for the growth of Au precursors. For comparison, an N-O-C catalyst was produced without Ni single atoms using a similar pyrolysis method. By introducing Au precursors with different concentrations, the Au_x/Ni-N-O-C (x=0.25, 0.50 or 0.75) catalysts were generated through low-temperature pyrolysis under an Ar atmosphere. The proportion of Ni and Au loading in Ni-N-O-C and $Au_{0.5}$/Ni-N-O-C samples was determined through inductively coupled plasma optical emission spectrometry (ICP-OES) and is detailed in Supplementary Table 3. Additionally, $Au_{0.5}$/N-O-C catalyst was fabricated using N-O-C as the substrate via a similar method.

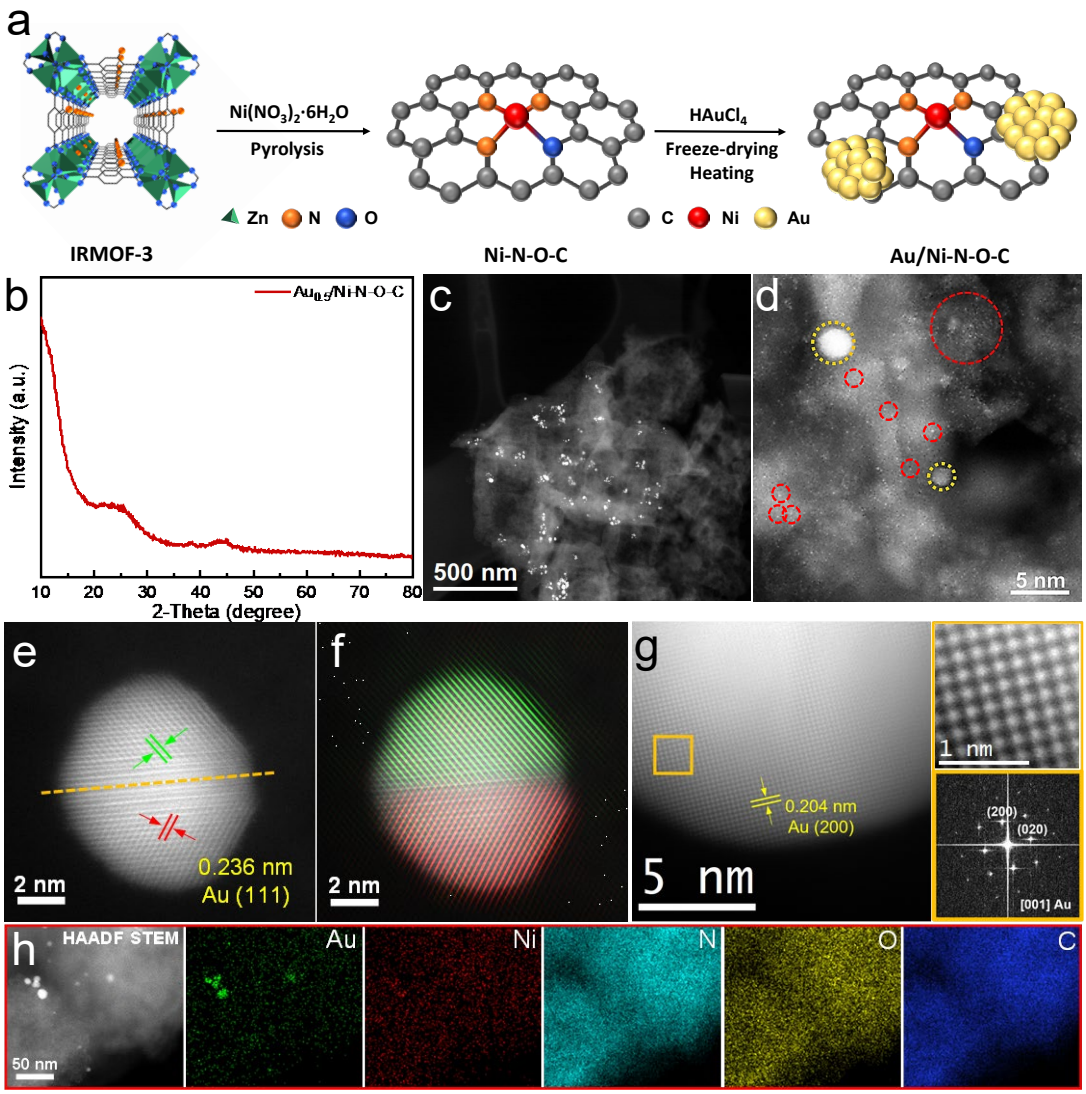

Fig. 2 Synthesis and characterization of Au/Ni-N-O-C. a Schematic illustration of the synthetic process. **b** XRD pattern, **c** low magnification and **d** high magnification AC HAADF-STEM image. **e** AC HAADF-STEM image of one of the Au nanoparticles in $Au_{0.5}$/Ni-N-O-C sample. The twin boundary in the middle (marked with an orange dashed line) divides the core into two semi spheres. **f** shows the colored twinned (111) planes in the upper (green) and bottom (red) hemispheres in the frequency filtered map of **e**. **g** AC HAADF-STEM image of one of the Au nanoparticles with a magnified detail and its corresponding indexed power spectrum. **h** HAADF-STEM image and representative EDS chemical composition maps.

Following pyrolysis, the crystal structures of N-O-C and Ni-N-O-C substrates were analyzed using XRD (Supplementary Fig. 5). Notably, these samples displayed distinct similarities in their diffraction patterns, exhibiting two broad peaks around 24° and 44°. These peaks corresponded to the (002) and (100) diffraction planes for

graphite carbon, indicating the presence of a carbon matrix in the samples after pyrolysis.[31,32] Moreover, the characteristic peaks associated with metal hybrids were notably absent in the XRD patterns of N-O-C and Ni-N-O-C, supporting that no metal crystalline species formed before the decoration with Au. Raman spectra of N-O-C and Ni-N-O-C samples, as presented in Supplementary Fig. 6, exhibited primary peaks at approximately 1365 and 1590 cm^{-1}, corresponding to the typical defect (D) and graphite (G) bands of graphitic carbon. The I_D/I_G band intensity ratio (1.1) in both samples was consistent, indicating a similar number of defects in both structures.[33,34] The presence of rich structural defects stemmed from vaporized ZnO_4 clusters.[35,36] In the cases of the $Au_{0.5}$/N-O-C and Au_x/Ni-N-O-C samples, a small new diffraction peak corresponding to the Au (111) plane was observed, indicating the successful introduction of Au particles into the N-O-C or Ni-N-O-C substrates (Fig. 2b and Supplementary Fig. 7). Meanwhile, the XRD patterns (Supplementary Fig.7b) demonstrated an increase in the yield of crystalline Au particles with the elevated concentration of the Au precursor in Au_x/Ni-N-O-C.

The morphology, structure, and elemental distribution of samples were characterized using aberration corrected (AC) high angle annular dark field (HAADF) scanning transmission electron microscopy (STEM). The low-magnification HAADF-STEM images shown in Fig. 2c and Supplementary Fig. 8 demonstrate that all samples transformed into sheet-like morphology, indicating that the pyrolysis process alters the original structure of the MOF precursors. Notably, the absence of bright nanoparticles/clusters in N-O-C and Ni-N-O-C samples suggests no Ni nanoparticle

or cluster formation after pyrolysis, aligning with the XRD results. Compared with the low-magnification HAADF STEM images of N-O-C and Ni-N-O-C in Supplementary Fig. 8, small bright nanoparticles were observed on $Au_{0.5}$/Ni-N-O-C shown in Fig. 2c at the same magnification, revealing the successfully introduction of Au nanoparticles on the $Au_{0.5}$/Ni-N-O-C catalyst. Local AC HAADF STEM images of different samples (Fig. 2d and Supplementary Figs. 9, 10) were employed to directly identify the distribution of single Ni atoms. The different Z contrast among Ni, N, O, and C elements allowed for the clear identification of homogeneously distributed Ni single sites (encircled by red dotted lines), further supporting the successful anchoring of Ni single atoms in both the $Au_{0.5}$/Ni-N-O-C and Ni-N-O-C samples. Furthermore, Fig. 2d and Supplementary Fig. 9 confirm the presence of some Au nanoparticles (encircled by yellow dotted line). A more in-depth examination of the Au nanoparticles displays well-defined lattice fringes of Au (111) and Au (002) planes (Fig. 2e-g). Energy dispersive X-ray spectroscopy (EDS) mapping results for $Au_{0.5}$/Ni-N-O-C and Ni-N-O-C samples are illustrated in Fig. 2h and Supplementary Fig. 11. These mappings not only reveal the uniform distribution of Ni, N and O dispersed throughout the carbon matrix but also clearly identify the presence of Au nanoparticles, encircled by Ni species. In addition, EDS mapping results of $Au_{0.5}$/N-O-C show obvious Au signals on N-O-C substrate (Supplementary Fig. 12).

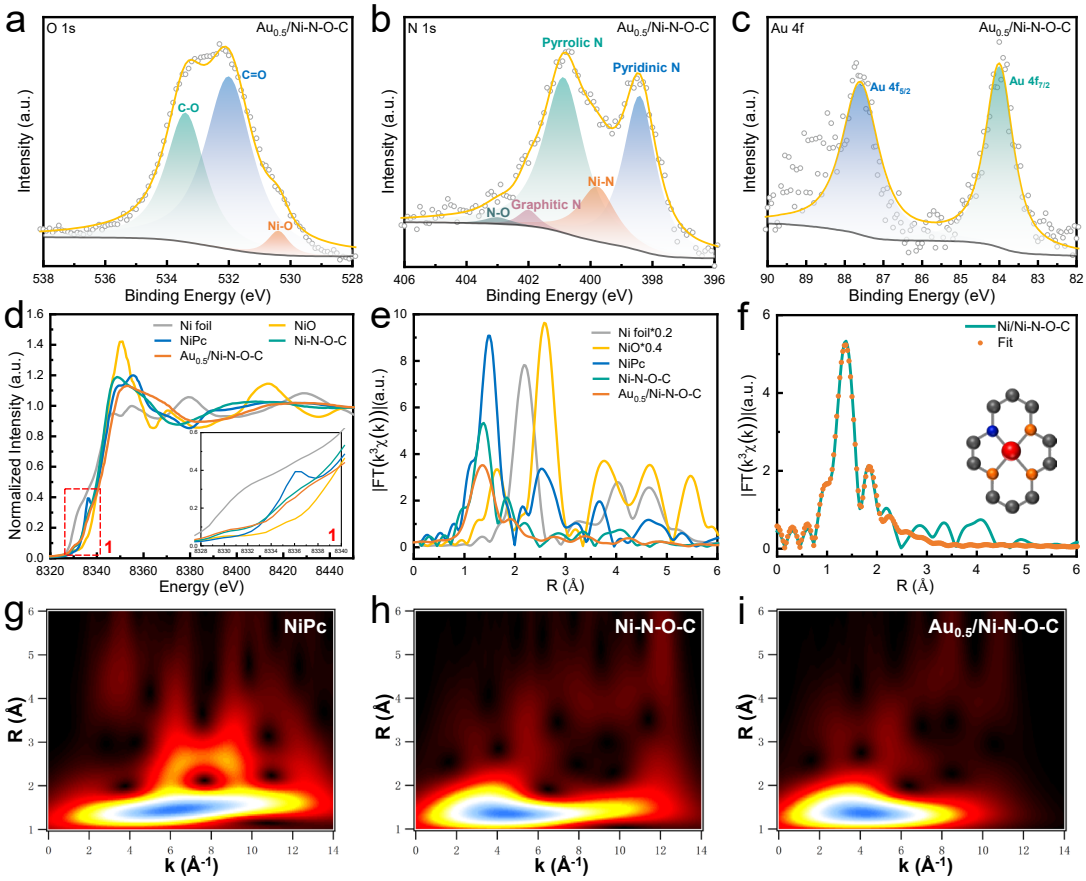

Fig. 3. Electronic structure characterization of catalysts. a-c High-resolution XPS **a** O 1s, **b** N 1s and **c** Au 4f spectrum of $Au_{0.5}$/Ni-N-O-C. **d** XANES spectra of the Ni-N-O-C and $Au_{0.5}$/Ni-N-O-C at Ni K-edge. The insets in **d** are the magnified corresponding regions. **e** EXAFS spectra at Ni K-edge on Ni-N-O-C and $Au_{0.5}$/Ni-N-O-C. **f** The corresponding Ni K-edge EXAFS fitting parameters for Ni-N-O-C sample. (Ni, O, N, C atoms are represented in red, blue, orange, and grey, respectively). **g-h** WT-EXAFS **g** NiPc, **h** Ni-N-O-C and **i** $Au_{0.5}$/Ni-N-O-C.

X-ray photoelectron spectroscopy (XPS) analysis has been used to identify the potential bonding structure and local chemical configuration of N-O-C, Ni-N-O-C and $Au_{0.5}$/Ni-N-O-C. When compared to the N-O-C sample without the introduction of Ni single atoms, a distinctive peak at 530.5 eV appears in the high-resolution O 1s spectroscopy of Ni-N-O-C and $Au_{0.5}$/Ni-N-O-C. This peak is attributed to Ni-O bond, potentially suggesting the retention of Ni-O chelation post-calcination (Fig. 3a and Supplementary Fig. 13). Notably, a porphyrin-like moiety at 399.7 eV, corresponding to the Ni-N coordination, can be observed in both Ni-N-O-C and $Au_{0.5}$/Ni-N-O-C,

supporting the presence of atomically dispersed Ni sites in both samples (Fig. 3b and Supplementary Fig 14).[37,38] These findings strongly suggest that the isolated Ni atoms are coordinated with N and O atoms in Ni-N-O-C and $Au_{0.5}$/Ni-N-O-C samples. This observation could be further confirmed by the X-ray absorption spectroscopy (XAS). The C 1s XPS spectra for all samples, as displayed in Supplementary Fig. 15, reveal three distinct peaks at binding energies of 284.5, 285.4 and 288.3 eV. These correspond to graphitic sp^2 carbon (C=C), carbon coordinated with doped O and N (C-N and C-O), and C=O bonds, respectively, indicating a common origin of these samples from the same MOFs precursors.[39,40] In Fig. 3c and Supplementary Fig. 17, a spin-orbit doublet for Au 4f at 84.0 eV and 87.7 eV is evident, signifying the zero-valence state of Au successfully introduced onto the Ni-N-O-C/N-O-C substrate after the low-temperature pyrolysis.[41]

Furthermore, XAS were conducted at the Ni K-edge for Ni-N-O-C, $Au_{0.5}$/Ni-N-O-C, and different reference samples to confirm the local coordination structure and valence of the atomically dispersed Ni. The X-ray absorption near edge structure (XANES) K-edge spectra of nickel phthalocyanine (NiPc), Ni-N-O-C, and $Au_{0.5}$/Ni-N-O-C exhibit similar characteristic features, which fall between those of metallic Ni foil and NiO reference, suggesting that the valence state of the Ni in NiPc, Ni-N-O-C and $Au_{0.5}$/Ni-N-O-C ranges between 0 and +2 (Fig. 3d).[25,42,43] In the inset of Fig. 3d, the pre-edge feature peak at approximately 8330 eV is assigned to the 1s → 3d transition of the central Ni atoms. This transition is typically forbidden in centrosymmetric point groups.[44] In comparison to the weak peak observed in planar

complexes NiPc, exhibiting a high D_{4h} centrosymmetry, there is an increase in peak intensity observed in Ni-N-O-C and $Au_{0.5}$/Ni-N-O-C, which is due to p-d mixing in non-centrosymmetric geometries.[44-46] Regarding the 1s → $4p_z$ transition near 8336 eV, NiPc showed a distinct transition characteristic of square-planar MN_4 moieties. However, the intensity of this transition in Ni-N-O-C and $Au_{0.5}$/Ni-N-O-C is weaker because of the distorted D_{4h} symmetry of the Ni atom.[24,47,48] The D_{4h} symmetry in Ni-N-O-C and $Au_{0.5}$/Ni-N-O-C is distorted due to the replaced oxygen in the lateral coordination. Meanwhile, a noticeable decrease in intensity is observed in $Au_{0.5}$/Ni-N-O-C compared to Ni-N-O-C, suggesting a higher distortion of isolated Ni atoms in $Au_{0.5}$/Ni-N-O-C due to the electron tug effect (inset of Fig. 3d). The Fourier transform (FT) k^2-weighted $\chi(k)$ functions of the Ni K-edge EXAFS of different samples are displayed in Fig. 3e. All samples exhibit a primary peak at approximately 1-2 Å, attributed to the first metal-metal/N/O shell. The first Ni-N/O coordination shell at 1.40 Å in Ni-N-O-C and $Au_{0.5}$/Ni-N-O-C catalysts differs significantly from Ni foil (Ni-Ni path at 2.1 Å) and NiO (Ni-O path at 1.60 Å).[49,50] Additionally, the absence of metallic Ni-Ni scattering supports the atomically dispersed nature of single Ni sites in prepared Ni-N-O-C and $Au_{0.5}$/Ni-N-O-C catalysts.[51] Compared to NiPc, the peak positions slightly shift leftward on Ni-N-O-C and $Au_{0.5}$/Ni-N-O-C, indicating a change in the coordination configuration of mixed Ni-N and Ni-O forms.[27,52] To further elucidate the detailed atomic structure of Ni-N-O-C, quantitative extend X-ray adsorption fine structure (EXAFS) analyses were performed, and the fitting results are shown in Fig. 3f. Based on the fitting outcomes and the corresponding parameters

listed in Supplementary Table 4, the coordination number of the Ni-N-O-C catalyst is determined to be 4 (comprising three bond lengths of 1.87 Å for Ni-N and one bond length of 2.12 Å for Ni-O). More information of the radial distance k-space resolution was obtained by wavelet transform (WT) EXAFS analysis (Fig. 3g-i and Supplementary Fig. 18). The WT contour at ≈4 $Å^{-1}$ for Ni-N-O-C and $Au_{0.5}$/Ni-N-O-C is close to NiO and moving toward NiPc, indicating the presence of atomically dispersed Ni-N sites and Ni-O coordination.[28] Therefore, the spectra obtained on the Ni-N-O-C sample are fitted assuming the presence of $Ni_1N_3O_1$ sites, consistent with the preceding analyses, which is expected to bring desirable catalytic performance.

2.3 Electrochemical CO_2-to-CO performance evaluation

The catalysts' electrochemical performances for CO_2 reduction were evaluated in a CO_2-saturated 0.5 M $KHCO_3$ solution using a standard three-electrode H-cell. To initially assess the eCO_2RR, linear sweep voltammetry (LSV) curves were conducted for all samples. Supplementary Fig. 19 and Fig. 4a illustrate an increased current density in CO_2-saturated solutions compared to those in Ar-saturated electrolytes, confirming the electrochemical reduction of CO_2 on N-O-C, Ni-N-O-C, $Au_{0.5}$/N-O-C and $Au_{0.5}$/Ni-N-O-C samples.[53-55] Moreover, in comparison to N-O-C and $Au_{0.5}$/N-O-C, both Ni-N-O-C and $Au_{0.5}$/Ni-N-O-C exhibited increased current density within the measured potential range, highlighting the significant role of the single Ni active sites in eCO_2RR. Notably, it is important to mention that $Au_{0.5}$/Ni-N-O-C displayed the smallest onset potential among the four catalysts, indicating a higher eCO_2RR catalytic activity. Gas products were regularly analyzed via online gas

chromatography (GC), revealing that CO and H_2 were the primary gases obtained across all samples. Additionally, the liquid-phase products of $Au_{0.5}$/Ni-N-O-C were examined using nuclear magnetic resonance (^{1}H-NMR) spectroscopy after the electrochemical CO_2 reduction processes. These analyses demonstrated the absence of any liquid products (Supplementary Fig. 20).

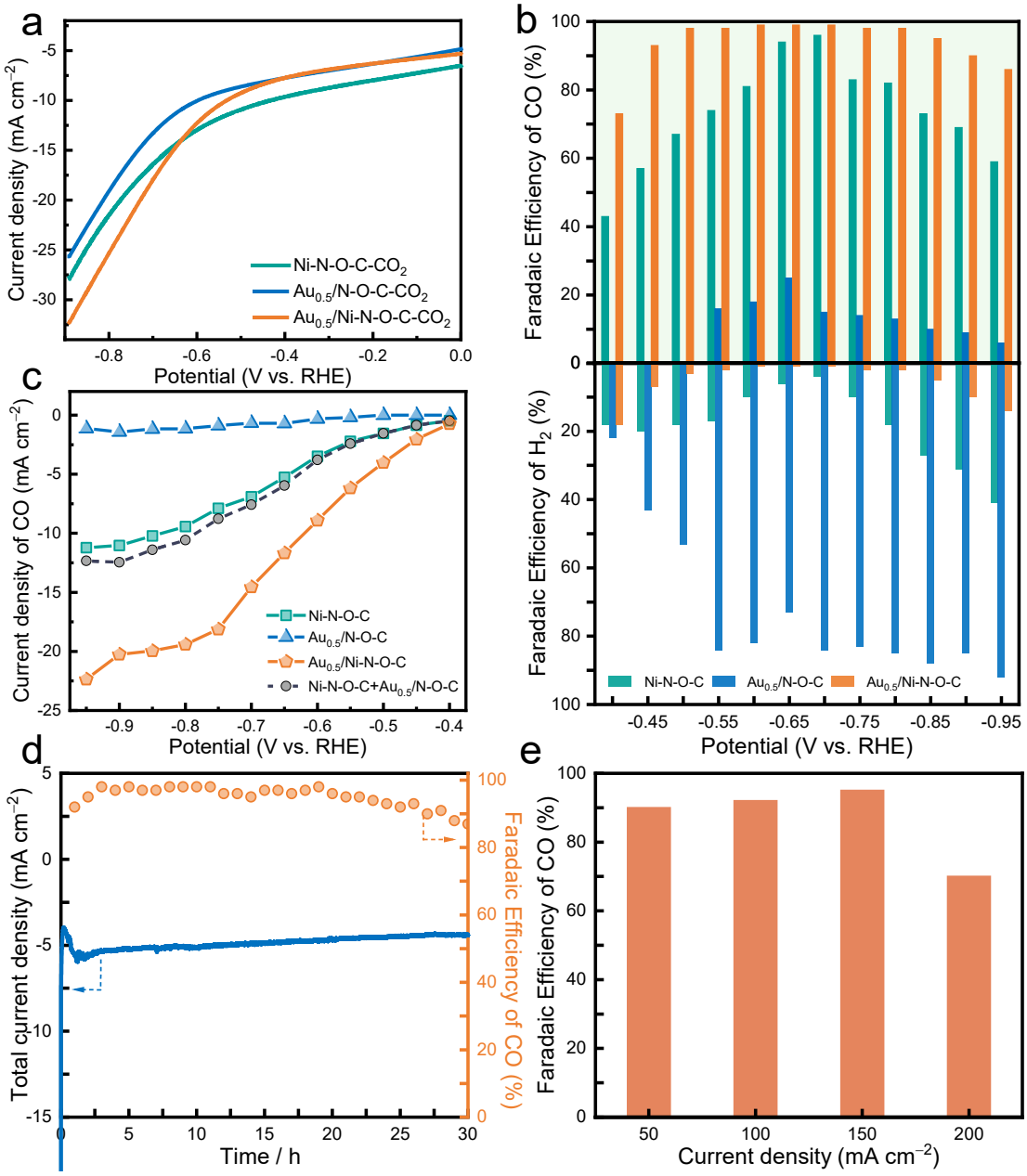

Fig. 4. Electrochemical CO_2RR Performances. a LSV curves. **b** Faradaic efficiencies (upper panel: FE_{CO}; bottom panel: FE_{H_2}).**c** Current density for CO production. **d** Stability test of $Au_{0.5}$/Ni-N-O-C at −0.50 V vs. RHE. **e** FE_{CO} on the $Au_{0.5}$/Ni-N-O-C catalyst in the range of current

densities from 50 to 200 mA cm^{-2} in a flow cell configuration with 1.0 M $KHCO_3$ as electrolyte.

Subsequently, potentiostatic electrolysis of CO_2 at different potentials was employed to further scrutinize the catalytic performances within a range from −0.40 to −0.95 V vs. RHE. The total current density measured for N-O-C, Ni-N-O-C, $Au_{0.5}$/N-O-C and $Au_{0.5}$/Ni-N-O-C samples is summarized in Supplementary Fig. 21. Under the same catalyst mass loading (approximately 1 mg cm^{-2}), the $Au_{0.5}$/Ni-N-O-C demonstrated the highest current density on each applied potential compared to N-O-C, $Au_{0.5}$/N-O-C, and Ni-N-O-C catalysts. This suggests that the enhanced activity of $Au_{0.5}$/Ni-N-O-C is mainly attributed to the electron tug effect of lateral O substitution and Au nanoparticles. The Faradaic efficiency (FE) for CO production was assessed within the potential range from −0.40 to −0.95 V (vs. RHE) for all synthesized catalysts, as shown in Fig. 4b (top panel) and Supplementary Fig. 22a. The increased FE of CO on Ni-N-O-C compared to N-O-C suggests the crucial role of Ni single atoms in eCO_2RR. Typically, for most single-atom catalysts reported, the FE_{CO} tends to decline rapidly after the optimal potential. Interestingly, $Au_{0.5}$/Ni-N-O-C catalyst showed continuous maintenance of high FE_{CO} (95%) under a broad potential range (−0.50 to −0.85 V vs. RHE), outperforming Ni-N-O-C, $Au_{0.5}$/N-O-C, and N-O-C throughout the potential window. Additionally, when compared to previously reported Ni-based SACs or Au-based electrocatalysts (Supplementary Fig. 31 and Table 5), the $Au_{0.5}$/Ni-N-O-C electrocatalyst exhibited a lower overpotential (340 mV) to achieve FE_{CO} > 90% and a broader potential window with FE_{CO} surpassing 95%. This supports the notion that the electron tug effect plays a pivotal role in enhancing eCO_2RR and overcoming

limitations in improving eCO_2RR performance on Ni-based SACs. The turnover frequency (TOF) of CO production for Ni-N-O-C and $Au_{0.5}$/Ni-N-O-C was calculated based on the current density of eCO_2 RR and the FE of CO. A larger TOF on $Au_{0.5}$/Ni-N-O-C (4000 h^{-1}) confirmed an intrinsically higher eCO_2RR activity in comparison to Ni-N-O-C. The above analysis showed that the kinetics for Ni-N-O-C has been improved by the introduction of Au nanoparticles via the electron tug effect (Supplementary Fig. 23). The CO current density of the $Au_{0.5}$/Ni-N-O-C catalyst surpassed that of Ni-N-O-C and $Au_{0.5}$/N-O-C on each applied potential (Fig. 4c), and even exceeded their combined value (dash line). This revelation suggests that the improved CO selectivity of $Au_{0.5}$/Ni-N-O-C is not merely a result of the composite effect of Ni single atoms and Au nanoparticles but is primarily attributed to the novel effect induced by the presence of Au nanoparticles and the Ni single sites. This observation is further corroborated by the catalytic performance obtained from the $Au_{0.5}$/Ni-N-O-C-physical mixture sample (Supplementary Fig. 24). In contrast to the $Au_{0.5}$/Ni-N-O-C, the $Au_{0.5}$/Ni-N-O-C-physical mixture sample displayed a decreased FE_{CO} at all applied potentials. However, it still exhibited a similar trend in FE_{CO}, which further demonstrates the interplay formed between Au nanoparticles and Ni SACs. As the potential shifted towards a more negative value, the FE(CO)s for Ni-N-O-C, $Au_{0.5}$/N-O-C and N-O-C gradually decreased since the competitive hydrogen evolution reaction (HER) became the dominant reaction, evident in the FE (H_2) shown in Fig. 4b (bottom panel) and Supplementary Fig. 22a. However, the FE(CO) of $Au_{0.5}$/Ni-N-O-C decreased negligibly as the potential became more negative. When

potential reached −0.95 V vs. RHE, the FE (CO) still maintained 86%. The potential-dependent H_2 current densities for the different catalysts are illustrated in Supplementary Figs. 22b and 25. These comparisons further demonstrate that electron tug effect in $Au_{0.5}$/Ni-N-O-C achieving electron redistribution around active sites can significantly enhance both high catalytic activity and selectivity to produce CO over a broad potential range. Notably, the $Au_{0.5}$/Ni-N-O-C catalyst demonstrated remarkable stability, maintaining nearly unchanged current density values and an FE_{CO} of over 85% after 30 hours of electrolysis at −0.50 V vs. RHE (Fig. 4d). As shown in Supplementary Fig. 26, XRD measurements were performed on $Au_{0.5}$/Ni-N-O-C coated on the carbon paper (CP) both before and after the electrocatalysis. No noticeable difference in the crystal structure was observed after the electrocatalysis test in 0.5 M $KHCO_3$, confirming that the primary structure of $Au_{0.5}$/Ni-N-O-C remained unchanged. To further reveal the viability of the $Au_{0.5}$/Ni-N-O-C catalyst, we examined its performance in a gas diffusion electrode (GDE)-based flow cell. This configuration aimed to achieve highly effective CO_2-to-CO conversion over the $Au_{0.5}$/Ni-N-O-C catalyst at industrial current density by mitigating the mass transport limitation of CO_2 gas. The $Au_{0.5}$/Ni-N-O-C catalyzed eCO_2RR in the flow cell could maintain more than 90% FE_{CO} values under a range of current densities from 50 to 150 mA cm^{-2}, indicating the promising applicability of $Au_{0.5}$/Ni-N-O-C for industrial eCO_2RR (Fig. 4e). These results demonstrate the industrial superiority and practicality of this catalyst. However, it is important to note that at a current density of 200 mA cm^{-2}, the FE of CO significantly dropped due to the unavoidable flooding of carbon

paper-based GDEs or the catalyst's destruction under high current density.

To elucidate the reason behind the enhanced catalytic performance of $Au_{0.5}$/Ni-N-O-C, we initially excluded the contribution of electrochemical surface area (ECSA) derived from double layer capacitance (C_{dl}), as summarized in Supplementary Fig. 27a-e. The slope in these graphs could serve as a reference for ECSA. Ni-N-O-C displayed the same C_{dl} (28 $mFcm^{-2}$) as N-O-C (28 $mFcm^{-2}$) but exhibited higher selectivity, indicating that the isolated Ni single metal active sites in Ni-N-O-C are the primary catalytic sites. This comparison revealed that introducing atomically dispersed metal sites into the N-O-C substrate significantly enhanced the activity of eCO_2RR.[14,15] However, both $Au_{0.5}$/N-O-C and $Au_{0.5}$/Ni-N-O-C samples displayed relatively smaller C_{dl} values (19 $mFcm^{-2}$ and 20 $mFcm^{-2}$, respectively). This suggests that introducing Au nanoparticles into the catalysts blocked some active sites in the original Ni-N-O-C or N-O-C. Despite this, $Au_{0.5}$/Ni-N-O-C exhibited higher selectivity compared to Ni-N-O-C. This observation implies that the intrinsic catalytic activity of $Au_{0.5}$/Ni-N-O-C does not linearly correlate with high ECSA.[12] More likely, the eCO_2RR catalytic properties of $Au_{0.5}$/Ni-N-O-C arise from the higher intrinsic activity of the Ni active site adjacent to the Au nanoparticles, underscoring the positive influence of Au nanoparticles surrounded by Ni SACs in enhancing eCO_2RR activity. Moreover, Nyquist plots revealed that the $Au_{0.5}$/Ni-N-O-C and Ni-N-O-C samples had lower interfacial charge-transfer resistance (R_{CT}) compared to N-O-C and $Au_{0.5}$/N-O-C. This reduction in resistance could favor the charge-transfer process from the Ni active sites to the adsorbed CO_2, facilitating the formation of intermediates (see Supplementary

Fig. 27f).[42] Additionally, various Au_x/Ni-N-O-C catalysts with different Au contents are shown in Supplementary Fig. 28. These results demonstrate that the presence of a specific amount/density of Au nanoparticles indeed influences the generation of CO at different applied potentials. As a result, to attain the optimal activity of Au/Ni-N-O-C, it is crucial to adjust the quantity of Au reagent to a point where the formed electron tug effect could broad the potential range with high selectivity and activity toward CO.

2.4 Mechanism Studies

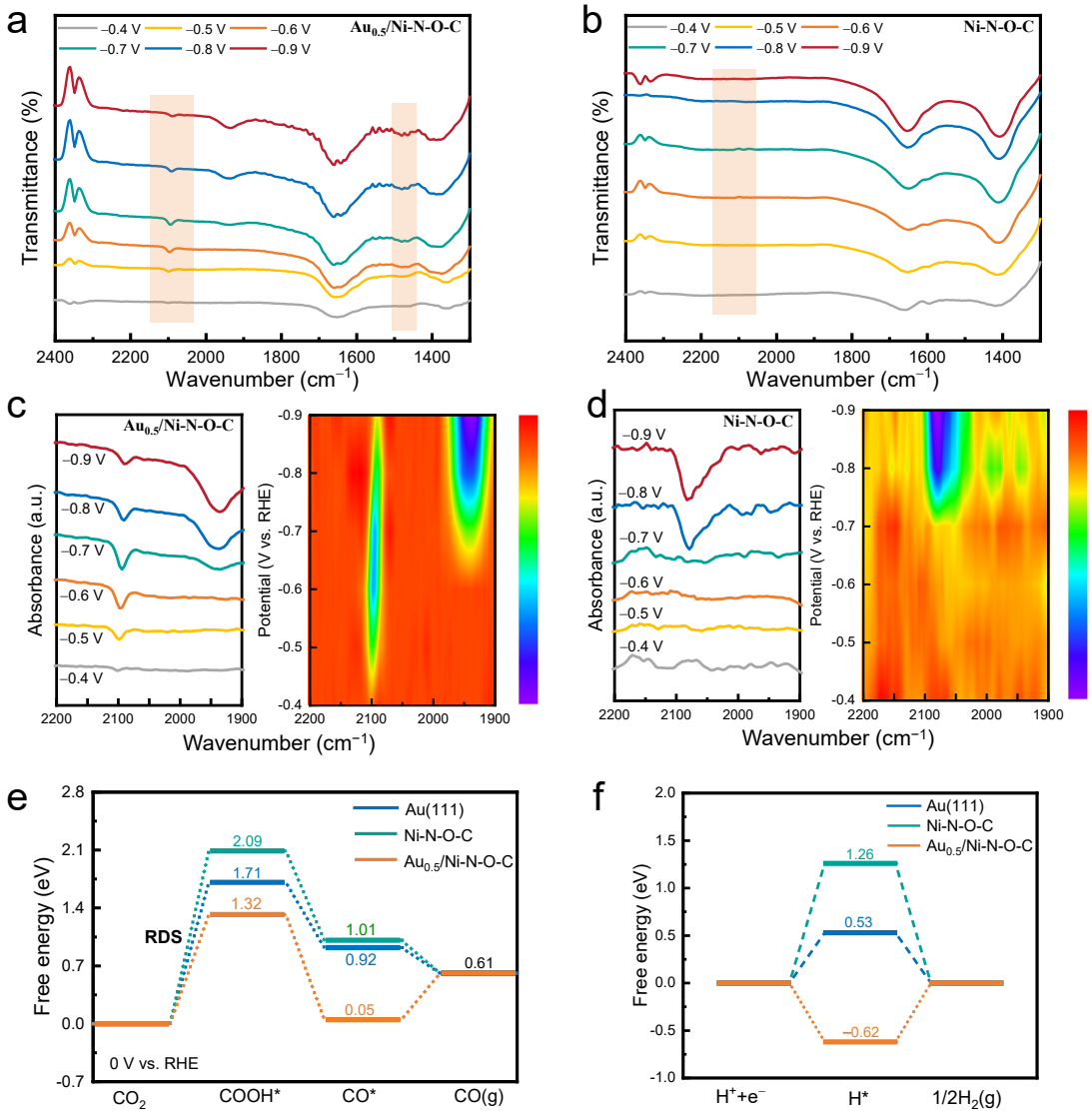

Fig. 5. *In-situ* ATR-IR analysis and DFT calculations. a, b *In-situ* ATR-IR spectra of **a** $Au_{0.5}$/Ni-N-O-C and **b** Ni-N-O-C. **c, d** High resolution *In-situ* ATR-IR analysis of **c** $Au_{0.5}$/Ni-N-O-C and **d** Ni-N-O-C. **e, f** Free energy profiles for the **e** eCO_2 RR to CO and **f** HER at 0 V (vs. RHE)

on simulated models.

Theoretical calculations have indicated that *COOH and *CO serve as important intermediates for CO formation. To specifically detect absorbed intermediate species and comprehend the reaction mechanisms, *in-situ* attenuated total reflection surface enhanced infrared absorption spectroscopy (ATR-SEIRAS) was conducted on Ni-N-O-C and $Au_{0.5}$/Ni-N-O-C samples during potential stepwise sweeping from −0.40 V to −0.90 V vs. RHE in a CO_2-saturated 0.5 M $KHCO_3$ solution. Several absorbance bands were observed between 2400 and 1000 cm^{-1} for both samples (Fig. 5a, b). Notably, there was no distinct band at 1830 cm^{-1}, linked to the vibration feature of bridge-bonded CO (CO_B), throughout the entire potential window, suggesting the presence of atomically dispersed sites as the active sites.[56] Two obvious peaks shown in Fig. 5a, b centered at 2350 cm^{-1} and 1650 cm^{-1} are indicative of the consumption of CO_2 and adsorbed H_2O in the solution, respectively.[47] Peaks around 1461 and 2100 cm^{-1} can be assigned to the adsorbed *COOH and *CO intermediate, respectively, which are the main reaction intermediates during the eCO_2RR.[56-58] However, noticeably increased intensities of *COOH peaks on $Au_{0.5}$/Ni-N-O-C appeared at a relatively low applied potential (from −0.40 V vs. RHE), suggesting that the *COOH intermediate was more easily generated on $Au_{0.5}$/Ni-N-O-C at a lower potential during eCO_2RR. Moreover, on the $Au_{0.5}$/Ni-N-O-C sample, the peaks at 2010 cm^{-1} appeared at potentials as low as −0.40 V vs. RHE and persisted at −0.90 vs. RHE, indicating the rapid protonation of *COOH to form *CO species at a low applied potential (Fig. 5c). In contrast, as shown in Fig. 5d, the *CO band was only obviously present on the Ni-

N-O-C sample at a relatively high potential (from −0.70 vs. RHE). These results indicate that the enhanced eCO_2RR on $Au_{0.5}$/Ni-N-O-C is primarily linked to rapid protonation of *COOH to form *CO species.

The Density Functional Theory (DFT) calculations have been employed to further investigate the electrocatalytic mechanism of the enhanced eCO_2RR performance on the $Au_{0.5}$/Ni-N-O-C sample with an electron tug effect. Utilizing the characterizations mentioned above, simulation models were developed for single Ni sites embedded in N-doped carbon substrate, both with and without a coated Au surface on the single Ni atomic sites (NiN_3O) for $Au_{0.5}$/Ni-N-O-C and Ni-N-O-C. Additionally, as a parallel comparison, the Au (111) counterpart model was also simulated without introduction of Ni single atom sites. Supplementary Fig. 29 demonstrates three elemental steps in the CO_2-to-CO conversion, involving two proton/electron transfer steps: first, the protonation of a CO_2 molecule to COOH* formation ($CO_2 + H^+ + e^- + * \rightarrow *COOH$); followed by the subsequent conversion of COOH* to CO* and H_2O ($*COOH + H^+ + e^- \rightarrow *CO + H_2O$) and the desorption of formed CO* from the surface of active site, where * signifies the adsorption site on the catalyst surface.[15,59] Clearly, the binding energies of COOH* formation and CO* desorption are deemed the principal steps during the eCO_2RR. As shown in Fig. 5e, the free energy profiles of CO_2 reduction to CO on all models are presented. The ΔG for the first step ($G = G_{(*COOH)} - G_{(*+CO_2)}$) on the Ni-N-O-C model is 2.09 eV, indicating the challenging formation of COOH* on highly dispersed Ni sites. Conversely, the CO* desorption process is exothermic on Ni-N-O-C due to the weak binding of CO* on Ni active sites. In contrast, a decrease

in *COOH reaction free energy was observed over the Ni sites in $Au_{0.5}$/Ni-N-O-C (1.32 eV) compared to that over the Ni-N-O-C model. This suggests that the introduction of Au nanoparticles around the single Ni active sites promotes the formation of the COOH* intermediate. The lower free energy for *COOH implies a lower potential for CO_2 reduction to CO in the synthesized $Au_{0.5}$/Ni-N-O-C catalyst, aligning with our experimental results. The *CO formation from *COOH is a downhill process for $Au_{0.5}$/Ni-N-O-C. However, compared to Ni-N-O-C (0.40 eV), the *CO desorption process on $Au_{0.5}$/Ni-N-O-C requires overcoming 0.56 eV of desorption free energy. Taking these into account, it is suggested that the rate-determining step (RDS) on Ni single sites is *COOH. The free energy change of RDS over the $Au_{0.5}$/Ni-N-O-C (1.32 eV) is significantly lower than that over Ni-N-O-C (2.09 eV), indicating that the prepared $Au_{0.5}$/Ni-N-O-C exhibits superior catalytic activity for CO_2-to-CO conversion from a thermodynamics perspective, a conclusion further supported by the projected density of states (PDOS) obtained on Ni-N-O-C and $Au_{0.5}$/Ni-N-O-C surfaces (Supplementary Fig. 30). When there is an interaction between CO_2 and metal sites, the empty *d* orbitals can accept electrons from the highest occupied molecular orbital, and the occupied *d* orbitals can back-donate electrons to the lowest unoccupied molecular orbital. The calculated projected density of states suggests that the *d*-band center of $Au_{0.5}$/Ni-N-O-C is very close to the Fermi level compared to Ni-N-O-C, indicating easier charge donation from $Au_{0.5}$/Ni-N-O-C to the adsorbate, resulting in enhanced binding with the intermediates (*COOH) over the $Au_{0.5}$/Ni-N-O-C.[60] The formation of *COOH is a potential-limiting step due to the

high activation energy of CO_2 molecule. The lower *d*-band center of Ni-N-O-C indicates a weaker interaction between intermediates and active sites, in line with our experimental results. Additionally, as the primary competing reaction for eCO_2RR, HER is illustrated. The free energy profile in Fig. 5f suggests that compared to the Au (111) model (0.53 eV), relatively higher energies (1.26 eV and 0.62 eV, respectively) are required for the formation of H_2 on Ni-N-O-C and $Au_{0.5}$/Ni-N-O-C. This indicates that HER is more challenging on Ni sites, favoring high selectivity toward the eCO_2RR of Ni-N-O-C and $Au_{0.5}$/Ni-N-O-C, consistent with the experimental findings.

3. Conclusions

In summary, our study demonstrates that the electron tug effect around the single-atom active site, achieved through a combination strategy that alters the lateral coordination environment and adjusting metal-substrate electronic conjugation, effectively enhances the polarization of electron distribution around the Ni active site. Due to its robust electron tug effect, the obtained $Au_{0.5}$/Ni-N-O-C catalysts were experimentally proven to be much more active than most unmodified Ni SACs, showing a high FE (CO) at a low overpotential and an extraordinary wide potential range for producing CO over 95%. DFT calculations demonstrate that the synergetic effect from O lateral coordination and Au nanoparticles around the Ni active sites can adjust the geometric structure and shift the *d*-band center of Ni, thus decreasing the free energy change of COOH* formation on Ni centers, eventually resulting in high CO_2 conversion activity and selectivity. Engineering electrocatalysts to fine-tune their electronic and geometric properties is crucial for controlling the electron distribution

of the active center. This work provides a feasible engineering pathway by polarizing the electron structure of SACs to prepare new atomically dispersed metal electrocatalysts for high-efficiency CO_2 electroreduction.

Methods

Preparation of IRMOF-3

In this procedure, the fabrication process of IRMOF-3 follows the methodology reported in our previous work.[37] Specifically, 932 mg $Zn(NO_3)_2 \cdot 6H_2O$ was dissolved in 100 ml DMF under magnetic stirring at room temperature to create a homogeneous solution. Subsequently, 181 mg 2-aminoterphthalic acid was added to the above mixture and subjected to ultrasonication for several minutes at room temperature until a clear solution formed. The resulting homogeneous solution was then placed in a Teflon-lined stainless-steel autoclave and allowed to react at 100 ºC for 24 h. Upon cooling to room temperature, the powder was collected by centrifugation, and washed multiple times with DMF and ethanol to eliminate any organic and inorganic residues. The final products were subsequently dried under vacuum at 65 ºC for overnight.

Preparation of Ni-doped IRMOF-3

100 mg IRMOF-3 powder was dispersed in 10 ml of DMF under ultrasound for 10 min at room temperature. After achieving a homogeneous solution, a $Ni(NO_3)_2 \cdot 6H_2O$ aqueous solution (10 mg/ml, 50 μL) was gradually added dropwise into the above solution under ultrasound for 5 min at room temperature. Subsequently, the mixed solution was magnetically stirred at room temperature for 3 h. Following the reaction, the powder was collected through centrifugation, washed multiple times with DMF

and ethanol, and dried under vacuum at 65 ºC for overnight.

Preparation of N-O-C and Ni-N-O-C

The as-prepared Ni-doped IRMOF-3 (or IRMOF-3) powders were placed on a porcelain boat. Subsequently, the samples were introduced into a tube furnace and heated at 950 °C for 2 h with a heating rate of 5 °C min^{-1} under an Ar atmosphere to produce dispersed Ni-N-O-C or N-O-C without metal introduction.

Preparation of Au_x/Ni-N-O-C and Au/N-O-C

To obtain $Au_{0.5}$/Ni-N-O-C and Au/N-O-C, 20 mg Ni-N-O-C or N-O-C was dispersed in 6 mL water and vigorously sonicated for 1 h. Following this, 0.12 mL $AuCl_4$ solution (1 mg/0.6 mL) was slowly added dropwise into the above suspension under vigorous stirring for 30 min. The adsorbed Au precursor was then rapidly frozen using liquid nitrogen, followed by overnight freeze-drying. The resulting dried powder was heated at 200°C in a tube furnace under Ar gas flow for 2 h with a heating rate of 5 °C min^{-1}. Adjusting the volume of the Au precursor solution allowed for the creation of $Au_{0.25}$/Ni-N-O-C (0.06 mL) and $Au_{0.75}$/Ni-N-O-C (0.18 mL) using the same process as $Au_{0.5}$/Ni-N-O-C. Additionally, the procedure synthesizing Au/N-O-C was similar to that of $Au_{0.5}$/Ni-N-O-C but using N-O-C as the substrate instead of Ni-N-O-C.

Preparation of Physical Mixture $Au_{0.5}$/Ni-N-O-C (Labelled as $Au_{0.5}$/Ni-N-O-C-physical mixture)

To prepare the $Au_{0.5}$/Ni-N-O-C-physical mixture sample, the synthesis procedure was the same as that used for $Au_{0.5}$/Ni-N-O-C without the 200°C heating step.

All additional experimental and characterization details are provided in the

supplementary information, including XRD patterns, FTIR, SEM, TEM, HAADF-STEM, BET, TGA, ICP, Raman spectra, EXAFS, XPS, gas calibration, ^{1}H-NMR, FE (H_2/CO), CV, Tafel slopes, LSV, EIS and the DFT results.

Author contributions

X.H., T. Z., and J. A. conceived and designed the project. X.H. carried out the XRD, SEM, sample preparation, and XRD, SEM, FTIR, Raman, XPS data analysis as well as electrochemical experiments. X. H., P. C., M. H., M. V. P., A. M., R. E. D.-B., and J. A. carried out the TEM, HRTEM, HAADF STEM, EDX mapping, and the corresponding data analysis. C. Z, W. T. performed the DFT calculations. L. Z. performed the XAS measurements and the corresponding data analysis. X. H., T. Z. and J. A. prepared the first version of the manuscript, and all authors contributed the final version.

ACKNOWLEDGMENTS

The authors thank Guillaume Sauthier, Javier Saiz for the XPS spectrum and FTIR tests at ICN2. ICN2 acknowledges funding from Generalitat de Catalunya 2021SGR00457. This study is part of the Advanced Materials programme and was supported by MCIN with funding from European Union NextGenerationEU (PRTR-C17.I1) and by Generalitat de Catalunya. The authors thank support from the project NANOGEN (PID2020-116093RB-C43), funded by MCIN/ AEI/10.13039/501100011033/ and by "ERDF A way of making Europe", by the "European Union". AGM has received funding from Grant RYC2021 - 033479 - I funded by MCIN/AEI/ 10.13039/501100011033 and by European Union

NextGenerationEU/PRTR. ICN2 is supported by the Severo Ochoa program from Spanish MCIN / AEI (Grant No.: CEX2021-001214-S) and is funded by the CERCA Programme / Generalitat de Catalunya. W. T. acknowledges for the financial support from the National Natural Science Foundation of China (Grant No. 22108070) and the Young Elite Scientists Sponsorship Program by CAST (No. 2022QNRC001). ER-C and ICN2 are founding members of e-DREAM.[61]

DECLARATION OF INTERESTS

The authors declare no competing interests.

References

1. Ding J*, et al.* A tin-based tandem electrocatalyst for CO_2 reduction to ethanol with 80% selectivity. *Nat. Energy*, DOI: 10.1038/s41560-023-01389-3 (2023).
2. Gao W, Xu Y, Fu L, Chang X, Xu B. Experimental evidence of distinct sites for CO_2-to-CO and CO conversion on Cu in the electrochemical CO_2 reduction reaction. *Nat. Catal.* **6**, 885-894 (2023).
3. Jiao J*, et al.* Constructing asymmetric double-atomic sites for synergistic catalysis of electrochemical CO_2 reduction. *Nat. Commun.* **14**, 6164 (2023).
4. Möller T, Filippi M, Brückner S, Ju W, Strasser P. A CO_2 electrolyzer tandem cell system for CO_2-CO co-feed valorization in a Ni-N-C/Cu-catalyzed reaction cascade. *Nat. Commun.* **14**, 5680 (2023).
5. Jin S, Hao Z, Zhang K, Yan Z, Chen J. Advances and Challenges for the Electrochemical Reduction of CO_2 to CO: From Fundamentals to Industrialization. *Angew. Chem. Int. Ed.* **60**, 20627-20648 (2021).
6. Schwarz HA, Dodson RW. Reduction potentials of CO_2- and the alcohol radicals. *J. Phys. Chem.* **93**, 409-414 (1989).
7. Qu Q, Ji S, Chen Y, Wang D, Li Y. The atomic-level regulation of single-atom site catalysts for the electrochemical CO_2 reduction reaction. *Chem. Sci.* **12**, 4201-4215 (2021).
8. Chen H, Fu W, Geng Z, Zeng J, Yang B. Inductive effect as a universal concept to design efficient catalysts for CO_2 electrochemical reduction: electronegativity difference makes a difference. *J. Mater. Chem. A* **9**, 4626-4647 (2021).
9. Wang Y*, et al.* Advanced Electrocatalysts with Single-Metal-Atom Active Sites. *Chem. Rev.* **120**, 12217-12314 (2020).
10. Wang J*, et al.* Atomically Dispersed Metal–Nitrogen–Carbon Catalysts with *d*-Orbital Electronic Configuration-Dependent Selectivity for Electrochemical CO_2-to-CO Reduction. *ACS Catal.* **13**, 2374-2385 (2023).
11. Hu X-M*, et al.* Selective CO_2 Reduction to CO in Water using Earth-Abundant Metal and Nitrogen-Doped Carbon Electrocatalysts. *ACS Catal.* **8**, 6255-6264 (2018).
12. Zhou S, Zhang L-J, Zhu L, Tung C-H, Wu L-Z. Amphiphilic Cobalt Phthalocyanine Boosts Carbon Dioxide Reduction. *Adv. Mater.* **35**, 2300923 (2023).
13. Zhou Y*, et al.* Asymmetric dinitrogen-coordinated nickel single-atomic sites for efficient CO_2 electroreduction. *Nat. Commun.* **14**, 3776 (2023).
14. Zhang T*, et al.* Quasi-double-star nickel and iron active sites for high-efficiency carbon dioxide electroreduction. *Energy Environ. Sci.* **14**, 4847-4857 (2021).
15. Ren W*, et al.* Isolated Diatomic Ni-Fe Metal–Nitrogen Sites for Synergistic Electroreduction of CO_2. *Angew. Chem. Int. Ed.* **58**, 6972-6976 (2019).
16. Varela AS, Ju W, Bagger A, Franco P, Rossmeisl J, Strasser P. Electrochemical Reduction of CO_2 on Metal-Nitrogen-Doped Carbon Catalysts. *ACS Catal.* **9**, 7270-7284 (2019).
17. Zhan Q-N, Shuai T-Y, Xu H-M, Zhang Z-J, Li G-R. Recent advances in the regulation of the coordination structures and environment of single-atom catalysts for carbon dioxide reduction reaction. *J. Mater. Chem. A* **11**, 7949-7986 (2023).

18. Qi Z, Zhou Y, Guan R, Fu Y, Baek J-B. Tuning the Coordination Environment of Carbon-Based Single-Atom Catalysts via Doping with Multiple Heteroatoms and Their Applications in Electrocatalysis. *Adv. Mater.* **35**, 2210575 (2023).
19. Zhang L*, et al.* Advances on Axial Coordination Design of Single-Atom Catalysts for Energy Electrocatalysis: A Review. *Nano-Micro Lett.* **15**, 228 (2023).
20. Leverett J*, et al.* Impurity Tolerance of Unsaturated Ni-N-C Active Sites for Practical Electrochemical CO_2 Reduction. *ACS Energy Lett.* **7**, 920-928 (2022).
21. Hua W*, et al.* A hierarchical Single-Atom Ni-N_3-C catalyst for electrochemical CO_2 reduction to CO with Near-Unity faradaic efficiency in a broad potential range. *Chem. Eng. J.* **446**, 137296 (2022).
22. Chen Z*, et al.* Achieving Efficient CO_2 Electrolysis to CO by Local Coordination Manipulation of Nickel Single-Atom Catalysts. *Nano Lett.* **23**, 7046-7053 (2023).
23. Qu M*, et al.* Rational design of asymmetric atomic Ni-P_1N_3 active sites for promoting electrochemical CO_2 reduction. *Nano Res.* **16**, 2170-2176 (2023).
24. Huang J-R*, et al.* Single-Product Faradaic Efficiency for Electrocatalytic of CO_2 to CO at Current Density Larger than 1.2 A cm^{-2} in Neutral Aqueous Solution by a Single-Atom Nanozyme. *Angew. Chem. Int. Ed.* **61**, e202210985 (2022).
25. Li X*, et al.* Convergent paired electrosynthesis of dimethyl carbonate from carbon dioxide enabled by designing the superstructure of axial oxygen coordinated nickel single-atom catalysts. *Energy Environ. Sci.* **16**, 502-512 (2023).
26. Li Z*, et al.* Stabilizing highly active atomically dispersed NiN_4Cl sites by Cl-doping for CO_2 electroreduction. *SusMat.* **3**, 498-509 (2023).
27. Wang Q*, et al.* Attenuating metal-substrate conjugation in atomically dispersed nickel catalysts for electroreduction of CO_2 to CO. *Nat. Commun.* **13**, 6082 (2022).
28. Li H*, et al.* Highly Dispersed NiO Clusters Induced Electron Delocalization of Ni-N-C Catalysts for Enhanced CO_2 Electroreduction. *Adv. Funct. Mater.* **33**, 2208622 (2023).
29. He Y*, et al.* Low-temperature strategy toward Ni-NC@Ni core-shell nanostructure with Single-Ni sites for efficient CO_2 electroreduction. *Nano Energy* **77**, 105010 (2020).
30. Zhang T*, et al.* Regulating electron configuration of single Cu sites via unsaturated N,O-coordination for selective oxidation of benzene. *Nat. Commun.* **13**, 6996 (2022).
31. Zeng Q*, et al.* Effects of nitrogen and oxygen on electrochemical reduction of CO_2 in nitrogen-doped carbon black. *Carbon* **202**, 1-11 (2023).
32. Li W, Zhang S, Guo F, Yu R, Chen Q, Zhong Q. Co4N nanoparticles encapsulated in N-doped carbon framework for boosting electrochemical stability in quantum dot sensitized solar cells. *Mater. Today Sustain.* **21**, 100312 (2023).
33. An Z*, et al.* Highly active, ultra-low loading single-atom iron catalysts for catalytic transfer hydrogenation. *Nat. Commun.* **14**, 6666 (2023).
34. Dong J*, et al.* Continuous electroproduction of formate via CO_2 reduction on local symmetry-broken single-atom catalysts. *Nat. Commun.* **14**, 6849 (2023).
35. Ye L*, et al.* Highly Efficient Porous Carbon Electrocatalyst with Controllable N-Species Content for Selective CO_2 Reduction. *Angew. Chem. Int. Ed.* **59**, 3244-3251 (2020).
36. Zhao D*, et al.* Atomic-level engineering $Fe_1N_2O_2$ interfacial structure derived from oxygen-abundant metal–organic frameworks to promote electrochemical CO_2 reduction. *Energy Environ. Sci.* **15**, 3795-3804 (2022).

37. Zhang T, *et al.* Site-Specific Axial Oxygen Coordinated FeN_4 Active Sites for Highly Selective Electroreduction of Carbon Dioxide. *Adv. Funct. Mater.* **32**, 2111446 (2022).
38. Chen Z, *et al.* Amination strategy to boost the CO_2 electroreduction current density of M–N/C single-atom catalysts to the industrial application level. *Energy Environ. Sci.* **14**, 2349-2356 (2021).
39. Yuan C-Z, *et al.* Tuning the activity of N-doped carbon for CO_2 reduction via in situ encapsulation of nickel nanoparticles into nano-hybrid carbon substrates. *J. Mater. Chem. A* **7**, 6894-6900 (2019).
40. Abbas SA, Song JT, Tan YC, Nam KM, Oh J, Jung K-D. Synthesis of a Nickel Single-Atom Catalyst Based on $Ni–N_{4–x}C_x$ Active Sites for Highly Efficient CO_2 Reduction Utilizing a Gas Diffusion Electrode. *ACS Appl. Energy Mater.* **3**, 8739-8745 (2020).
41. Kruse N, Chenakin S. XPS characterization of Au/TiO_2 catalysts: Binding energy assessment and irradiation effects. *Appl. Catal. A: Gen.* **391**, 367-376 (2011).
42. Zhao C, *et al.* Solid-Diffusion Synthesis of Single-Atom Catalysts Directly from Bulk Metal for Efficient CO_2 Reduction. *Joule* **3**, 584-594 (2019).
43. An B, *et al.* Liquid Nitrogen Sources Assisting Gram-Scale Production of Single-Atom Catalysts for Electrochemical Carbon Dioxide Reduction. *Adv. Sci.* **10**, 2205639 (2023).
44. Martini A, *et al.* Tracking the Evolution of Single-Atom Catalysts for the CO2 Electrocatalytic Reduction Using Operando X-ray Absorption Spectroscopy and Machine Learning. *J. Am. Chem. Soc.* **145**, 17351-17366 (2023).
45. Li R, *et al.* Polystyrene Waste Thermochemical Hydrogenation to Ethylbenzene by a N-Bridged Co, Ni Dual-Atom Catalyst. *J. Am. Chem. Soc.* **145**, 16218-16227 (2023).
46. Kim YE, *et al.* Atomically Dispersed Nickel Coordinated with Nitrogen on Carbon Nanotubes to Boost Electrochemical CO_2 Reduction. *ACS Energy Lett.* **8**, 3288-3296 (2023).
47. Huang M, *et al.* Template-Sacrificing Synthesis of Well-Defined Asymmetrically Coordinated Single-Atom Catalysts for Highly Efficient CO_2 Electrocatalytic Reduction. *ACS Nano* **16**, 2110-2119 (2022).
48. Wang X, *et al.* Dynamic Activation of Adsorbed Intermediates via Axial Traction for the Promoted Electrochemical CO_2 Reduction. *Angew. Chem. Int. Ed.* **60**, 4192-4198 (2021).
49. Chen J, *et al.* Dual Single-Atomic $Ni-N_4$ and $Fe-N_4$ Sites Constructing Janus Hollow Graphene for Selective Oxygen Electrocatalysis. *Adv. Mater.* **32**, 2003134 (2020).
50. Gong Y-N, *et al.* Regulating the Coordination Environment of MOF-Templated Single-Atom Nickel Electrocatalysts for Boosting CO_2 Reduction. *Angew. Chem. Int. Ed.* **59**, 2705-2709 (2020).
51. Pei J, *et al.* N-Bridged Co–N–Ni: new bimetallic sites for promoting electrochemical CO_2 reduction. *Energy Environ. Sci.* **14**, 3019-3028 (2021).
52. Zhang J, *et al.* Tuning the Coordination Environment in Single-Atom Catalysts to Achieve Highly Efficient Oxygen Reduction Reactions. *J. Am. Chem. Soc.* **141**, 20118-20126 (2019).
53. Han X, *et al.* Engineering the Interfacial Microenvironment via Surface Hydroxylation to Realize the Global Optimization of Electrochemical CO_2 Reduction. *ACS Appl. Mater. Interfaces* **14**, 32157-32165 (2022).
54. Han X, *et al.* A MOF-Based Spatial-Separation Layer to Enable a Uniform Favorable

Microenvironment for Electrochemical CO_2 Reduction. *Small Struct.* **4**, 2200388 (2023).
55. Liang Z*, et al.* A novel π-d conjugated cobalt tetraaza[14]annulene based atomically dispersed electrocatalyst for efficient CO_2 reduction. *Chem. Eng. J.* **442**, 136129 (2022).
56. Qin X, Zhu S, Xiao F, Zhang L, Shao M. Active Sites on Heterogeneous Single-Iron-Atom Electrocatalysts in CO_2 Reduction Reaction. *ACS Energy Lett.* **4**, 1778-1783 (2019).
57. Ren X*, et al.* In-situ spectroscopic probe of the intrinsic structure feature of single-atom center in electrochemical CO/CO_2 reduction to methanol. *Nat. Commun.* **14**, 3401 (2023).
58. Chen J*, et al.* Promoting Electrochemical CO_2 Reduction via Boosting Activation of Adsorbed Intermediates on Iron Single-Atom Catalyst. *Adv. Funct. Mater.* **32**, 2110174 (2022).
59. Zhu W*, et al.* Enhanced CO_2 Electroreduction on Neighboring Zn/Co Monomers by Electronic Effect. *Angew. Chem. Int. Ed.* **59**, 12664-12668 (2020).
60. Yang Y*, et al.* Theoretical Insights into Nitrogen-Doped Graphene-Supported Fe, Co, and Ni as Single-Atom Catalysts for CO_2 Reduction Reaction. *J. Phys. Chem. C* **126**, 4338-4346 (2022).
61. R. Ciancio, R. E. Dunin-Borkowski, E. Snoeck, M. Kociak, R. Holmestad, J. Verbeeck, A. I. Kirkland, G. Kothleitner, J. Arbiol, Microscopy and Microanalysis, 28, 2900-2902 (2022).